

This is the accepted manuscript made available via CHORUS. The article has been published as:

Magnetic order induces symmetry breaking in the single-crystalline orthorhombic CuMnAs semimetal

Eve Emmanouilidou, Huibo Cao, Peizhe Tang, Xin Gui, Chaowei Hu, Bing Shen, Junyi Wu, Shou-Cheng Zhang, Weiwei Xie, and Ni Ni

Phys. Rev. B **96**, 224405 — Published 4 December 2017

DOI: [10.1103/PhysRevB.96.224405](https://doi.org/10.1103/PhysRevB.96.224405)

Magnetic order induces symmetry breaking in the single crystalline orthorhombic CuMnAs semimetal

Eve Emmanouilidou,¹ Huibo Cao,² Peizhe Tang,³ Xin Gui,⁴ Chaowei Hu,¹
Bing Shen,¹ Junyi Wu,¹ Shou-Cheng Zhang,^{3,5} Weiwei Xie,⁴ and Ni Ni^{1,*}

¹*Department of Physics and Astronomy and California NanoSystems Institute,
University of California, Los Angeles, CA 90095, USA*

²*Quantum Condensed Matter Division, Oak Ridge National Laboratory, Oak Ridge, TN 37831, USA*

³*Department of Physics, McCullough Building, Stanford University, Stanford, California 94305-4045, USA*

⁴*Department of Chemistry, Louisiana State University, Baton Rouge, Louisiana 70803, USA*

⁵*Stanford Institute for Materials and Energy Sciences,
SLAC National Accelerator Laboratory, Menlo Park, California 94025, USA.*

(Dated: November 15, 2017)

Recently, orthorhombic CuMnAs has been proposed to be a magnetic material where topological fermions exist around the Fermi level. Here we report the magnetic structure of the orthorhombic Cu_{0.95}MnAs and Cu_{0.98}Mn_{0.96}As single crystals. While Cu_{0.95}MnAs is a commensurate antiferromagnet below 360 K with a propagation vector of $\mathbf{k} = 0$, Cu_{0.98}Mn_{0.96}As undergoes a second-order paramagnetic to incommensurate antiferromagnetic phase transition at 320 K with $\mathbf{k} = (0.1, 0, 0)$, followed by a second-order incommensurate to commensurate antiferromagnetic phase transition at 230 K. In the commensurate antiferromagnetic state, the Mn spins order parallel to the crystallographic b -axis but antiparallel to their nearest-neighbors, with the spin orientation along the b axis. This magnetic order breaks S_{2z} , the two-fold rotational symmetry around the c axis, resulting in finite band gaps at the crossing point and the disappearance of the massless topological fermions. However, our first principles calculations suggest that orthorhombic CuMnAs can still host spin-polarized surface states and signature induced by non-trivial topology, which makes it a promising candidate for antiferromagnetic spintronics.

I. INTRODUCTION

Recently, a lot of research interest has focused on the physics of Dirac fermions in the bulk material systems. The existence of these excitations in condensed matter systems, which resemble massless fermions from high-energy physics, has been theoretically proposed and experimentally realized in numerous non-magnetic materials, including Cd₃As₂^{1,2}, Na₃Bi^{3,4}, etc. By breaking the inversion symmetry (\mathcal{P}) or the time-reversal symmetry (\mathcal{T}), a Dirac point can be split into a pair of Weyl points. To break \mathcal{T} , we can either apply an external magnetic field or use the spontaneous magnetic moment inside the material. In the latter case, the correlation between spontaneous magnetism and Weyl fermions has been studied in the AMnPn₂ (A = rare earth or alkali earth and Pn = Sb or Bi) system^{5–12}, the half-Heusler compound GdPtBi^{13,14} and suggested in CeSbTe¹⁵.

Magnetic CuMnAs compounds are proposed to host non-trivial topology^{16,17}. CuMnAs has two polymorphs; the tetragonal (TET) CuMnAs, which crystalizes in the space group $P4/nmm$, and the orthorhombic (ORT) CuMnAs crystalizing in the $Pnma$ space group. The TET phase consists of alternating layers of edge-sharing CuAs₄ and MnAs₄ tetrahedra. It has been proposed to be a candidate with favourable applications in spintronics^{18,19} and a topological metal-insulator transition driven by the Néel vector¹⁷. On the other hand, the ORT phase consists of a 3D network of edge-sharing CuAs₄ and MnAs₄ tetrahedra (Fig. 1(a)), where the Mn atoms form a 3D distorted honeycomb lattice (Fig. 1(b)).

ORT CuMnAs is proposed to be an antiferromagnetic topological massless Dirac semimetal even when the spin-orbit coupling (SOC) is fully considered¹⁶. The first principles calculation shows that based on the theoretically-determined magnetic structure, although both the \mathcal{T} and \mathcal{P} symmetries are broken, their combination \mathcal{PT} and the non-symmorphic screw symmetry S_{2z} , which is the two-fold rotational symmetry around the c axis, are preserved. Based on the above symmetry assumptions, a gapless Dirac point is robust in the reciprocal space. Thus, the antiferromagnetic (AFM) ORT CuMnAs provides an ideal system to study the interplay between AFM and Dirac fermions¹⁶.

In this paper, we focus on the ORT CuMnAs single crystals. The synthesis, resistivity and susceptibility of polycrystalline ORT CuMnAs have been previously reported elsewhere²⁰. However, although the magnetic structure of the ORT CuMnAs is crucial in the symmetry analysis to investigate the topology of the material, it has not yet been determined experimentally. Here we report the synthesis and characterization of single crystals of Cu _{x} Mn _{y} As. We experimentally determine its magnetic structure through neutron diffraction experiments, and find that it indeed breaks the \mathcal{T} and \mathcal{P} symmetries but keeps their combination \mathcal{PT} . However, since the experimentally determined magnetic order breaks the S_{2z} symmetry, massless Dirac fermions are no longer robust. Our first principles calculations further show that this magnetic order will cause ORT CuMnAs to host an interesting topological phase with spin-polarized surface states, which could be promising for spintronics applications.

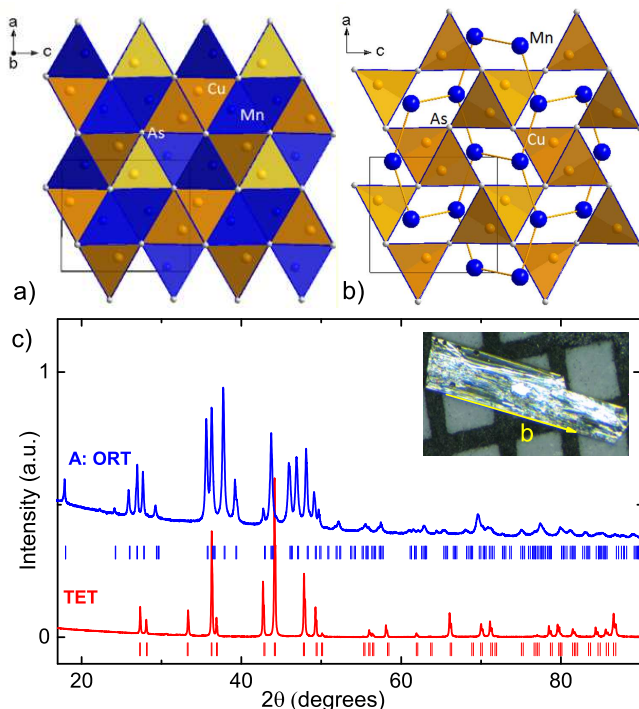


FIG. 1. (a), (b) The crystal structure of ORT CuMnAs. (a): the CuAs₄ (orange) and MnAs₄ (blue) tetrahedral building blocks. (b): The distorted Mn honeycomb lattice is indicated (Mn in blue). (c) Powder x-ray diffraction patterns of ORT (pulverized single crystals from batch A) and TET (from powder synthesis) phases. Ticks indicate the Bragg peak positions. Inset: A picture of an ORT single crystal against a mm sized grid. This as-grown surface is the *bc* plane.

II. MATERIAL SYNTHESIS AND EXPERIMENTAL METHODS

For the solid state reaction, Cu, Mn and As powders were mixed thoroughly and pressed into a pellet. The pellet was slowly heated to 600°C and kept at that temperature overnight. It was then heated to 1000°C, where it dwelled for 20 hours, and finally quenched in water. Through powder x-ray diffraction measurements (Fig. 1(c)) we found that stoichiometric or slightly less As leads to a pure ORT CuMnAs phase, while 6% of extra As results in the TET phase and a slight amount of MnAs.

CuMnAs single crystals were grown via the high temperature solution method with Bi as the flux^{21,22}. Cu shots, Mn granules, As and Bi chunks were mixed together and placed inside a 5-ml alumina crucible. The alumina crucible was then placed inside an evacuated quartz tube with 1/3 Atm of Ar gas. The ampoule was subsequently heated to 1100 °C, held for 3 h, cooled to 850° C in 2 hours and then cooled to 400°C at a rate of 3°C / h. We additionally allowed the crystals to anneal at 400°C for 0 or 24 hours before the single crystals were separated from the flux using a centrifuge.

Table I summarizes the starting growth concentrations we have tried and the resultant phases of the single crystals. The CuMnAs single crystals have a rectangular plate-like growth habit. The inset of Fig. 1(c) shows the picture of an ORT CuMnAs single crystal against a mm scale. Typical thickness of these single crystals is around 0.07 mm. The as-grown surface is the *bc* plane while the long axis of the plate is its *b* axis.

Single crystal X-ray diffraction data were collected on a Bruker Apex II X-ray diffractometer with Mo radiation k_α ($\lambda = 0.71073\text{\AA}$). Intensities were extracted and corrected for Lorentz and polarization effects with the SAINT program. Numerical absorption corrections were accomplished with XPREP which is based on face-indexed absorption²³. The twin unit cell was tested. With the SHELXTL package, the crystal structures were solved using direct methods and refined by full-matrix least-squares on F_2 ²⁴.

Single crystal neutron diffraction measurements were carried out on the HB-3A four-circle diffractometer at the High Flux Isotope Reactor (HFIR), Oak Ridge National laboratory (ORNL). The neutron wavelength of 1.546 Å from a bent Si-220 monochromator²⁵. The magnetic symmetry analysis was carried out on the Bilbao Crystallographic Server²⁶ and the data were refined with FullProf Suite²⁷.

Electrical resistivity, Hall coefficient and heat capacity data were collected using a Quantum Design Physical Property Measurement System (QD PPMS Dynacool). The standard four-probe configuration was used. The susceptibility was measured with a QD Magnetic Properties Measurement System (QD MPMS). Around 5 single crystals with similar phase transitions were selected for both heat capacity and susceptibility measurements.

The first principles calculations were carried out by density functional theory method with the projector augmented wave method²⁸, as implemented in the Vienna ab initio simulation package²⁹. The Perdew-Burke-Ernzerhof exchange-correlation functional and the plane wave basis with energy cutoff of 300 eV were employed. The inner atomic positions of the lattice were allowed to be fully relaxed until the residual forces are less than 1×10^{-3} eV/Å. The Monkhorst-Pack *k* points were $9 \times 15 \times 9$, and SOC was included in self-consistent electronic structure calculations. The maximally localized Wannier functions were constructed to obtain the tight-binding Hamiltonian³⁰, which is used to calculate the bulk Fermi surface, surface electronic spectrum and surface states.

III. EXPERIMENTAL RESULTS

The resistivities of the ORT single crystals we measured are around tenths of mΩ-cm and show metallic behavior. We observed two types of temperature-dependent resistivity behaviors from samples we measured from batch A to batch E. One type is with only one resistive

TABLE I. The growth conditions and crystal structure of $\text{Cu}_x\text{Mn}_y\text{As}$ single crystals. For more details of dR/dT , please refer to Fig. 2(a) and (b) and the supplementary material. * means although only one resistive anomaly was observed, the temperature where it occurred is much lower than 360 K, the one for polycrystalline sample.

Batch	Cu: Mn: As: Bi	Annealing time (h)	Structure	kinks in dR/dT
A	1 : 1 : 0.9 : 12	0	ORT	1
B	1 : 1 : 1 : 12	24	ORT	2
C	1 : 1 : 1.1 : 12	0	ORT	1* or 2
D	0.9 : 1 : 1 : 12	0	ORT	1* or 2
E	1.1 : 1 : 1 : 12	0	ORT	1*

anomaly, the other type shows two resistive anomalies. Figures 2(a)-(b) show the normalized resistivity curves of each type, $\rho(T)/\rho(400\text{K})$ of Piece A (PA) from batch A and Piece B (PB) from batch B. More temperature dependent resistance curves of each batch can be found in the supplementary materials³¹. Figure 2(a) shows only one resistivity drop in PA, suggesting the existence of one phase transition. The derivative of the resistivity, $d\rho/dT$, shows a sharp kink at 360 K. On the other hand, PB shows two resistive anomalies, suggesting the occurrence of two successive phase transitions. The $d\rho/dT$ plot indicates that one kink appears around 320 K and the other occurs around 230 K. Table I summarizes the number of resistivity anomalies in the ORT phase from each growth trial. From the summary and all temperature dependent resistivity curves we measured³¹, we can see the quality of the single crystal is very sensitive to the nominal concentration of Cu/Mn/As. Only when the starting As concentration is a little less than the stoichiometric concentration in the flux growth (batch A), the resulting single crystals show only one resistive anomaly around 360 K, consistent with the polycrystalline sample²⁰ and suggesting high quality of the sample. Even for batch E where only one resistive anomaly exists, the anomaly occurs around 300 K, which is 60 K lower than the one in the polycrystalline sample, suggesting poorer sample quality than the ones in batch A.

The inset of Fig. 2(a) shows the field dependent Hall resistivity $\rho_{yx}(H)$ of PA at 2 K and 100 K. ρ_{yx} is positive, indicating that holes dominate the transport. It is linearly proportional to H and shows almost no temperature dependence, suggesting the validity of the single band model here. Based on $n = B/e\rho_{yx}$, the estimated carrier density is $\approx 6.5 \times 10^{20}/\text{cm}^3$. This value is significantly greater than Dirac semimetals Cd_3As_2 ³², Na_3Bi ³³ and Weyl semimetal TaAs ³⁴, but comparable to the Dirac nodal-line semimetal candidates ZrSiSe ³⁵ and CaAgAs ³⁶.

The temperature dependent susceptibility ($M/H(T)$) and heat capacity ($C_p(T)$) of PB are presented in Figs. 2(c)-(d). Two slope changes can also be observed in the $M/H(T)$ data, which can be clearly seen in $d(M/H)/dT$. From 300 K to 400 K, the highest temperature we measured, the $M/H(T)$ data is almost temperature independent, showing no Curie-Weiss behavior. The $C_p(T)$ data

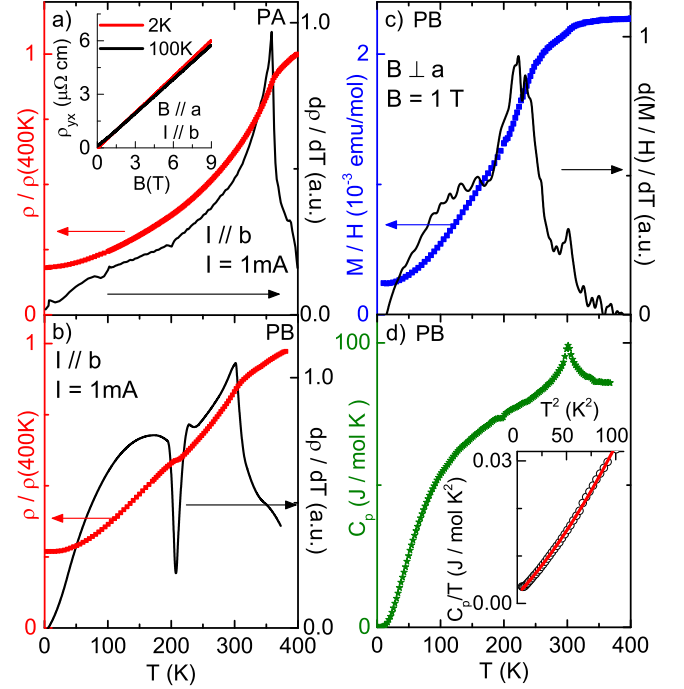


FIG. 2. PA: (a) The normalized resistivity $\rho/\rho(400\text{ K})$ and its derivative $d\rho/dT$ vs. T . Inset: The Hall resistivity ρ_{yx} vs. T . PB: (b)-(d): (b): The normalized resistivity $\rho/\rho(400\text{ K})$ and $d\rho/dT$ vs. T . (c): The susceptibility M/H and $d(M/H)/dT$ vs. T . (d) The heat capacity C_p vs. T . Inset: C_p/T vs. T^2 .

show only one heat capacity jump around 320 K without any anomaly at 230 K, suggesting that the phase transition at 230 K is most likely a transition between two ordered phases. Since both phase transitions are at high temperatures, we fitted the C_p/T data from 2 K to 10 K using $C_p = \gamma T + \alpha T^3 + \beta T^5$, where the first term refers to the electronic heat capacity and the rest to the low temperature lattice heat capacity. We deduced a Sommerfeld coefficient $\gamma = 1.88\text{ mJ mol}^{-1}\text{ K}^{-2}$ which indicates a small density of states at the Fermi level for the ORT CuMnAs .

To understand why the physical properties are so sensitive to the growth condition, single crystal X-ray and neutron diffraction measurements were performed on PA and PB to investigate their structural properties. No

TABLE II. Single crystal crystallographic data of PA and PB in the ORT $Pnma$ space group at 300 K.

CuMnAs	PA	PB
F.W. (g/mol)	190.22	190.05
$a(\text{\AA})$	6.5716(4)	6.5868(4)
$b(\text{\AA})$	3.8605(2)	3.8542(3)
$c(\text{\AA})$	7.3047(4)	7.3015(5)
$V(\text{\AA}^3)$	185.32(2)	185.36(6)
No. reflections; R_{int}	1624;0.0210	2189;0.0304
R_1 ; wR_2	0.0172; 0.0342	0.0227; 0.0459
Goodness of fit	1.154	1.047

structural phase transition is detected down to 100 K. To determine the stoichiometry of the samples, five different structural models were used in the refinement. Model I assumes vacancies on both Cu and Mn sites. Model II assumes Mn on Cu sites. Model III assumes Cu on Mn sites. Model IV assumes Cu vacancy and Cu on Mn sites. Model V assumes Mn vacancies and Mn on Cu sites. It turns out that Model I, II and III give the best refinements using single crystal X-ray diffraction data. Combined with the SEM-EDX data, which gives $\text{Cu}_{0.98(3)}\text{Mn}_{0.98(4)}\text{As}_{1.02(4)}$ for both PA and PB, we are convinced that both site vacancies and site disorders exist. Tables II and III summarize the refined crystal structure, atomic positions and site occupancies of PA and PB. The major difference between them is the stoichiometry. PA has fully occupied Mn sites with 5.0(2)% of Cu site vacancies, leading to a chemical formula of $\text{Cu}_{0.95}\text{MnAs}$, while PB has vacancies in both Cu and Mn sites with a chemical formula of $\text{Cu}_{0.98}\text{Mn}_{0.96}\text{As}$. In the rest of the paper, we will denote $\text{Cu}_{0.95}\text{MnAs}$ as PA and $\text{Cu}_{0.98}\text{Mn}_{0.96}\text{As}$ as PB. The difference in the physical properties between PA and PB most likely arises from the stoichiometry of the Mn and Cu sites. It is worth noting that due to the similar atomic number of Cu and Mn, it is hard to get reliable information on the Cu/Mn site disorder just by single crystal X-ray diffraction data. Therefore, the single crystal neutron diffraction data were used to investigate the extent of Cu/Mn site mixing here. Considering the number of vacancies revealed by single crystal X-ray diffraction, the refinement of the neutron diffraction data suggests 6% of site disorder in PB and 5% of site disorder in PA.

To unravel the nature of these phase transitions, we performed single crystal neutron diffraction experiments. Figure 3 (a) presents the rocking curve scan at (1,1,0) on PA. The fact that the peak shows up at (1,1,0) at 150 K but not at 400 K indicates long range antiferromagnetic order exists at 150 K. The temperature dependent (1,1,0) peak intensity agrees well with the $d\rho/dT$, shown in Fig. 3(b). It suggests a second order AFM phase transition and can be fitted using the power law $I(T)/I_0 = (M(T)/M_0)^2 = A + (1 - T/T_N)^{2\beta}$, where M_0 is the saturation moment. With $T_N = 360$ K, the crit-

TABLE III. Atomic coordinates and equivalent isotropic displacement parameters of PA and PB at 300 K. U_{eq} is defined as $1/3$ of the trace of the orthogonalized U_{ij} tensor (\AA^2).

Atom	Site	SOF	x	y	z	U_{eq}
PA: $\text{Cu}_{0.95}\text{MnAs}$						
Cu	4c	0.950(2)	0.37684(6)	1/4	0.05894(5)	0.0120(1)
Mn	4c	1	0.46024(7)	1/4	0.67737(6)	0.0121(2)
As	4c	1	0.25394(4)	1/4	0.37525(4)	0.0080(1)
PB: $\text{Cu}_{0.98}\text{Mn}_{0.96}\text{As}$						
Cu	4c	0.977(3)	0.3770(1)	1/4	0.0590(1)	0.0120(2)
Mn	4c	0.964(4)	0.4589(1)	1/4	0.6773(1)	0.0122(2)
As	4c	1	0.2544(1)	1/4	0.3754(1)	0.0079(1)

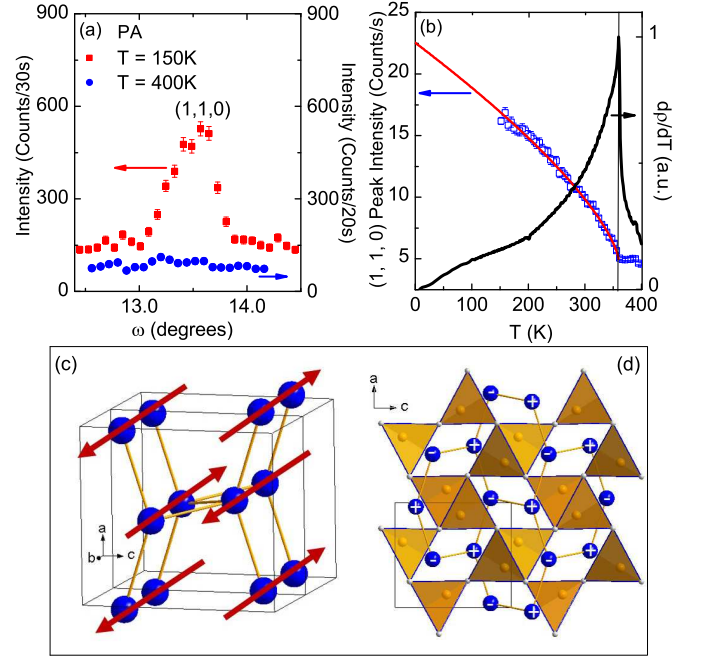


FIG. 3. (a) The (1,1,0) intensity vs. ω for PA. (b) A comparison between the (1,1,0) peak intensity and the $d\rho/dT$ vs. T . The red line is the power law fit, see text. (c) The magnetic structure of PA in the C-AFM state. Only the Mn sublattice is shown. (d) The view of the magnetic structure from the b direction. Mn atoms are shown in blue. “+” denotes spins pointing out of plane while “-” denotes spin pointing in plane.

ical exponent is $\beta = 0.35(3)$, which agrees with the ϕ^4 model in 3D³⁷ and suggests the breakdown of the mean field theory ($\beta = 0.5$) and thus a strong spin fluctuation near T_N . We refined the magnetic and nuclear structure of $\text{Cu}_{0.95}\text{MnAs}$ together based on 76 effective magnetic reflections. $Pn'ma$ is the only magnetic symmetry which can fit the data. The R-factor is 0.0508 and the goodness of fit is 6.08. The refined propagation vector is $\mathbf{k}=0$, indicating the commensurate antiferromagnetism (C-AFM) here³⁸ and the unit cell of the magnetic structure coincides with the crystal structure. Figures 3(c)-

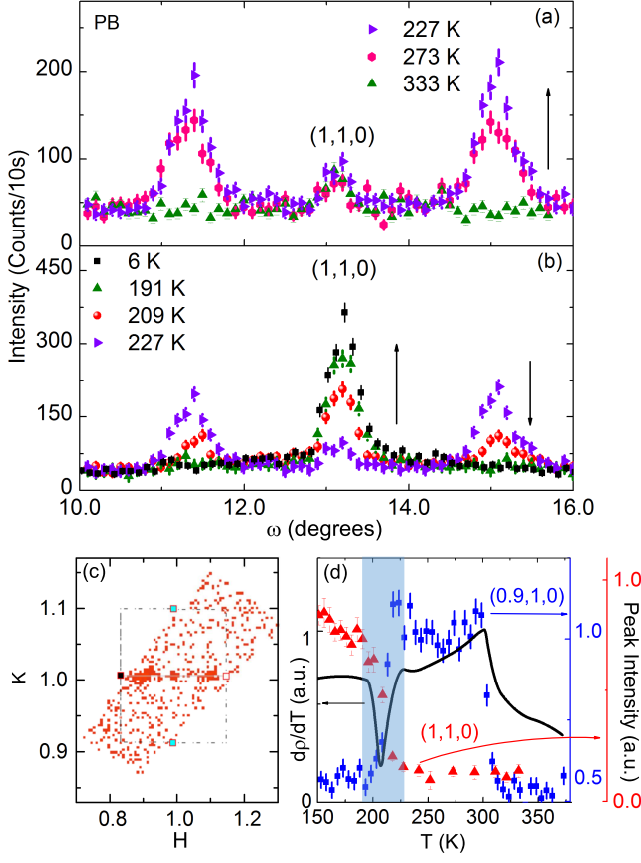


FIG. 4. (a)-(b): The intensity vs. ω for PB. The black arrows indicate the trend of the peak intensity with decreasing temperature. (c): A cut of the neutron scattering in the $hk0$ plane. (d) A comparison between the (0.9,1,0) peak intensity and $d\rho/dT$ vs. T . The light blue box marks the temperature region where C-AFM and IC-AFM compete and coexist.

(d) show the refined C-AFM structure. Mn spins sit on a distorted honeycomb sublattice and order parallel to each other along the b axis (Fig. 3 (c)) with the nearest-neighbor spins antiferromagnetically aligned to each other (Fig. 3(d)). This magnetic structure is the same as the one proposed theoretically in Ref.¹⁶, but with the spin orientation along the b axis. The refined magnetic moment at 150 K is $4.0(1) \mu_B/\text{Mn}$.

Figures 4(a) and (b) show the rocking curve scan at (1,1,0) on PB. The (1,1,0) peak is not allowed by the crystal structure symmetry in the ORT CuMnAs phase, and the non-zero intensity we observed above 320 K is due to the half-wavelength ($\lambda/2$) contamination of the neutron beam²⁵. The wavelength of 1.546 \AA we used at HB3A is selected by the Si-220 monochromator, which also picks the half-wavelength neutrons that make up 1.4% of the main beam flux at HB3A. In Fig. 4(a), magnetic satellite peaks begin to appear near the (1,1,0) as the sample is cooled below 320 K, suggesting incommensurate antiferromagnetism (IC-AFM)³⁸. Figure 4(c) shows a cut in the $hk0$ plane at 227 K. We can clearly detect the three

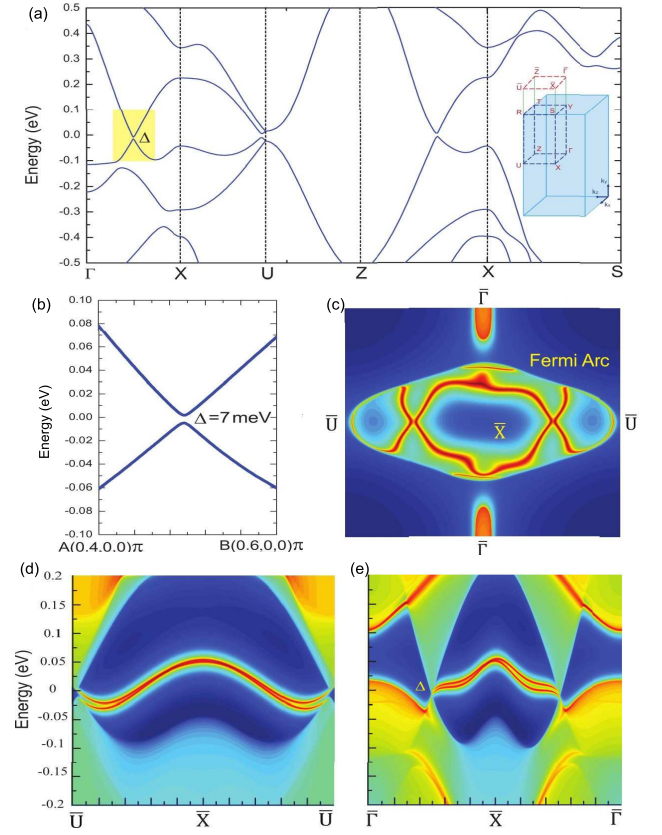


FIG. 5. (a) The calculated band structures of the ORT CuMnAs with SOC and the magnetic structure shown in Fig. 3(c). Inset is the Brillouin zone and its projection to the (010) surface. Δ is the band gap of massive topological fermion along ΓX line. (b) The zoom-in view of the band structure marked by yellow box in (a). (c) The Fermi surface contour on the (010) surface at the calculated Fermi level. The corresponding electronic spectra along (d) $k_x = \pi/a$ and (e) $k_z = 0$. The Fermi level is set to zero.

peaks shown in Fig. 4(a). The concentration of points at (0.9,1,0) and (1.1,1,0) indicates the presence of the incommensurate magnetic peaks, suggesting an incommensurate propagation vector $\mathbf{k} = (0.1,0,0)$. Upon further cooling of the sample below 230 K, we observe that both (0.9,1,0) and (1.1,1,0) peak intensities decrease while the (1,1,0) peak intensity starts to increase, indicating a competition between the C-AFM with the propagation vector $\mathbf{k} = 0$ and IC-AFM. Below 190 K, both (0.9,1,0) and (1.1,1,0) peaks diminish whereas the (1,1,0) peak keeps increasing, suggesting the disappearance of IC-AFM. To better visualize the competition and coexistence, Figure 4(d) shows the (0.9,1,0) and (1,1,0) peak intensities and $d\rho/dT$ as a function of temperature. We can see that $\text{Cu}_{0.98}\text{Mn}_{0.96}\text{As}$ undergoes a second-order paramagnetism (PM) to IC-AFM phase transition at 320 K as well as a second-order IC-AFM to C-AFM phase transition at 230 K. IC-AFM competes and coexists with the C-AFM phase between 230 to 190 K and disappears below 190

K. Based on 102 effective magnetic peaks, the refined C-AFM structure is the same as the one in $\text{Cu}_{0.95}\text{MnAs}$ (Figs. 3 (c)-(d)) with the refined magnetic moment at 6 K as $4.3(2) \mu_B/\text{Mn}$ and a R-factor of 0.0555. The moment is smaller than $5 \mu_B/\text{Mn}$, the theoretical saturation moment for Mn^{2+} .

IV. DISCUSSION

Based on the magnetic structure and easy axis determined experimentally, in order to explore the electronic and topological properties of ORT CuMnAs with the magnetic orientations along b axis, we recalculate its bulk band structures and the corresponding (010) surface states. Although no chemical disorder or vacancies are considered in the DFT calculation, since the material still holds the translational symmetry and maintains the ORT structures, the electronic structure and surface states shown in Fig. 5 should capture the main character. Due to the presence of the \mathcal{PT} symmetry in the experimental C-AFM phase, every bulk state is doubly degenerate. Furthermore, the band inversion still exists in this system, thus the non-trivial topological properties can appear. Because the C-AFM order breaks the non-symmorphic gliding symmetry R_y and screw symmetry S_{2z} , in contrast to the case with spin orientation along the c axis¹⁶, now the gapless coupled Weyl fermions disappear and the Dirac nodal line is fully gapped everywhere by SOC in the bulk Brillouin zone (BZ), as shown in Fig. 5(a). The gap size however is quite small. For example, the band gap induced by SOC along the ΓX line is just 7 meV, as indicated in Fig. 5(b). Figure 5(c) shows the spin-polarized surface states emerging from the gapped bulk states (see Fig. 5(d) and (e)) on the (010) side surface. Due to the absence of rotational symmetries on the (010) surface, the Fermi surface contour at the Fermi level is asymmetric, and the spin-polarized surface states are gapped. This distinguishing character is different from surface states in topological insulators and

Dirac semimetals. On the other hand, because the bulk Dirac fermions in this case are massive and the time reversal symmetry is broken, the fluctuations could resemble the dynamical axion field, which gives rise to exotic modulation of the electromagnetic field showing a similar signature to axion insulators³⁹.

V. CONCLUSION

In conclusion, the Dirac antiferromagnetic semimetal candidates, ORT $\text{Cu}_{0.95}\text{MnAs}$ and $\text{Cu}_{0.98}\text{Mn}_{0.96}\text{As}$ single crystals, show no structural phase transitions down to 100 K. The magnetism is very sensitive to the stoichiometry of the Cu and Mn sites. $\text{Cu}_{0.95}\text{MnAs}$ has a PM to C-AFM phase transition at 360 K while an intermediate IC-AFM state between PM and C-AFM states appears in $\text{Cu}_{0.98}\text{Mn}_{0.96}\text{As}$. In both C-AFM states, spins order parallel to one another along the b axis, but antiparallel to their Mn nearest-neighbors with the moment around $4.3 \mu_B/\text{Mn}$. The spin orientations are along the b axis, which break both S_{2z} and R_y symmetries in the C-AFM state and gap the coupled Weyl nodes and Dirac nodal line, resulting in similar electromagnetic response to that of axion insulators. Furthermore, the presence of spin-polarized surface states on this AFM semimetal makes ORT CuMnAs to be a good candidate for the antiferromagnetic spintronic applications.

Work at UCLA was supported by the U.S. Department of Energy (DOE), Office of Science, Office of Basic Energy Sciences under Award Number DE-SC0011978. Work at ORNL's High Flux Isotope Reactor was sponsored by the Scientific User Facilities Division, Office of Basic Energy Sciences, DOE. The research at LSU was supported by the LSU-startup funding and Louisiana Board of Regents Research Competitiveness Subprogram under the Contract Number LEQSF (2017-20)-RD-A-08. PZ and SCZ acknowledge FAME, one of six centers of STARnet, a Semiconductor Research Corporation program sponsored by MARCO and DARPA. NN thanks Dr. Yilin Wang for useful discussion.

* Corresponding author: nini@physics.ucla.edu

¹ S. Borisenko, Q. Gibson, D. Evtushinsky, V. Zabolotnyy, B. Buchner, and R. J. Cava, Phys. Rev. Lett. **113**, 027603 (2014)

² M. Neupane, S.-Y. Xu, R. Sankar, N. Alidoust, G. Bian, C. Liu, I. Belopolski, T.-R. Chang, H.-T. Jeng, H. Lin et al., Nat. Commun. **5**, 3786 (2014)

³ Z. K. Liu, B. Zhou, Y. Zhang, Z. J. Wang, H. M. Weng, D. Prabhakaran, S.-K. Mo, Z. X. Shen, Z. Fang, X. Dai et al., Science **343**, 864 (2014)

⁴ J. Xiong, S. K. Kushwaha, T. Liang, J. W. Krizan, M. Hirschberger, W. Wang, R. J. Cava, and N. P. Ong, Science **350**, 413 (2015)

⁵ K. Wang, D. Graf, H. Lei, S.W. Tozer, and C. Petrovic,

Phys. Rev. B **84**, 220401 (2011)

⁶ K. Wang, D. Graf, L. Wang, H. Lei, S.W. Tozer, and C. Petrovic, Phys. Rev. B **85**, 41101 (2012)

⁷ K. Wang, D. Graf, and C. Petrovic, Phys. Rev. B **87**, 235101 (2013)

⁸ S. Borisenko, D. Evtushinsky, Q. Gibson, A. Yaresko, T. Kim, M.N. Ali, B. Büchner, M. Hoesch, and R.J. Cava, arXiv:1507.04847v2, Unpublished, (2015)

⁹ J.Y. Liu, J. Hu, Q. Zhang, D. Graf, H.B. Cao, S.M.A. Radmanesh, D.J. Adams, Y.L. Zhu, G. F. Cheng, X. Liu, et. al, arXiv:1507.07978v2, Unpublished, (2015)

¹⁰ J. Liu, J. Hu, H. Cao, Y. Zhu, A. Chuang, D. Graf, D.J. Adams, S.M.A. Radmanesh, L. Spinu, I. Chiorescu, and Z. Mao, Sci. Rep. **6**, 30525 (2016)

- ¹¹ H. Masuda, H. Sakai, M. Tokunaga, Y. Yamasaki, A. Miyake, J. Shiogai, S. Nakamura, S. Awaji, A. Tsukazaki, H. Nakao, et. al, *Sci. Adv.* **2**, (2016)
- ¹² S. Huang, J. Kim, W.A. Shelton, E.W. Plummer, and R. Jin, *Proc. Natl. Acad. Sci.* **114**, 6256 (2017)
- ¹³ M. Hirschberger, S. Kushwaha, Z. Wang, Q. Gibson, S. Liang, C.A. Belvin, B.A. Bernevig, R.J. Cava, and N.P. Ong, *Nat. Mater.* **15**, 1161 (2016)
- ¹⁴ T. Suzuki, R. Chisnell, A. Devarakonda, Y.-T. Liu, W. Feng, D. Xiao, J.W. Lynn, and J.G. Checkelsky, *Nat. Phys.* **12**, 1119 (2016)
- ¹⁵ Leslie M. Schoop, Andreas Topp, Judith Lippmann, Fabio Orlandi, Lukas Muechler, Maia G. Vergniory, Yan Sun, Andreas W. Rost, Viola Duppel, Maxim Krivenkov, Shweta Sheoran, Pascal Manuel, Andrei Varykhalov, Binghai Yan, Reinhard K. Kremer, Christian R. Ast, Bettina V. Lotsch, Unpublished, arxiv: 1707.03408 (2017)
- ¹⁶ P. Tang, Q. Zhou, G. Xu, S.-C. Zhang, *Nat. Phys.* **12**, 1100 (2016)
- ¹⁷ L. Šmejkal, J. Železný, J. Sinova, and T. Jungwirth, *Phys. Rev. Lett.* **118**, 106402 (2017)
- ¹⁸ P. Wadley, V. Hills, M. R. Shahedkhah, K. W. Edmonds, R. P. Champion, V. Novák, B. Ouladdiaf, D. Khalyavin, S. Langridge, V. Saidl, et. al, *Sci. Rep.* **5**, 17079 (2015)
- ¹⁹ P. Wadley, B. Howells, J. Železný, C. Andrews, V. Hills, R. P. Champion, V. Novák, K. Olejník, F. Maccherozzi, S. S. Dhesi et. al, *Science* **351**, 587-590 (2016)
- ²⁰ F. Máca, J. Mašek, O. Stelmakhovich, X. Martí, H. Reichlová, K. Uhlirová, P. Beran, P. Wadley, V. Novák, and T. Jungwirth, *J. Magn. Magn. Mater.* **324**, 1606 (2012)
- ²¹ P. C. Canfield and Z. Fisk, *Philos. Mag. B* **65**, 1117 (1992)
- ²² K. Uhlirová, R. Tarasenko, F. JavierMartínez-Casado, B. Vondracková, Z. Matěj, *J. Alloys Compd.*, 650, 224 (2015)
- ²³ SHELXTL, version 6.10, Bruker AXS Inc.: Madison, WI, 2000.
- ²⁴ G. M. Sheldrick, *Acta Crystallogr. A* **64**, 112-122 (2008)
- ²⁵ B. C. Chakoumakos, H. Cao, F. Ye, A.D. Stoica, M. Popovici, M. Sundaram, W. Zhou, J.S. Hicks, G.W. Lynn, R.A. Riedel, "Four-circle single-crystal neutron diffractometer at the High Flux Isotope Reactor", *J. Appl. Crystallogr.* **44**, 655-658 (2011)
- ²⁶ J. M. Perez-Mato, S. V. Gallego, E. S. Tasci, L. Elcoro, G. de la Flor, and M. I. Aroyo, *Annu. Rev. Mater. Res.* **45**, 217 (2015)
- ²⁷ J. Rodríguez-Carvajal, *Phys. B Condens. Matter* **192**, 55 (1993), program available at www.ill.fr/dif/Soft/fp/
- ²⁸ P. E. Blöchl, *Phys. Rev. B* **50**, 17953 (1994)
- ²⁹ G. Kresse and J. Furthmüller, *Phys. Rev. B* **54**, 11169 (1996)
- ³⁰ A. A. Mostofi, J. R. Yates, Y.-S. Lee, I. Souza, D. Vanderbilt and N. Marzari, *Comput. Phys. Commun.* **178**, 685 (2008)
- ³¹ E. Emmanouilidou, et. al, see supplementary materials.
- ³² T. Liang, Q. Gibson, M. N. Ali, M. Liu, R. J. Cava, and N. P. Ong, *Nat. Mater.* **14**, 280 (2014)
- ³³ J. Xiong, S. Kushwaha, J. Krizan, T. Liang, R. J. Cava, and N. P. Ong, *Europhys. Lett.* **114**, 27002 (2016)
- ³⁴ C. L. Zhang, S.-Y. Xu, I. Belopolski, Z. Yuan, Z. Lin, B. Tong, G. Bian, N. Alidoust, C.-C. Lee, S.-M. Huang et. al, *Nat. Comm.* **7**, 10735 (2016)
- ³⁵ J. Hu, Z. Tang, J. Liu, X. Liu, Y. Zhu, D. Graf, K. Myhro, S. Tran, C. N. Lau, J. Wei et. al, *Phys. Rev. Lett.* **117**, 016602 (2016)
- ³⁶ E. Emmanouilidou, B. Shen, X. Deng, T.-R. Chang, A. Shi, G. Kotliar, S.-Y. Xu, and N. Ni, *Phys. Rev. B* **95**, 245113 (2017)
- ³⁷ G.A. Baker, B.G. Nickel, and D.I. Meiron, *Phys. Rev. B* **17**, 1365 (1978)
- ³⁸ T. Chatterji, in *Neutron Scattering from Magnetic Materials*, edited by T. Chatterji (Elsevier, Amsterdam, 2006). J. M. Smith, in *Molecular Dynamics*, edited by C. Brown (Academic, New York, 1980).
- ³⁹ R. Li, J. Wang, X.-L. Qi and S.-C. Zhang, *Nat. Phys.* **6**, 284 (2010)